UNIVERSITY OF CALIFORNIA SAN DIEGO

Horizontal Coherence Function for Ambient Noise and Helicopter Sound in Water

A Thesis submitted in partial satisfaction of the requirements
for the degree Master of Science

in

Electrical Engineering (Applied Ocean Sciences)

by

Hong Jie Kok

Committee in charge:

Professor Michael J. Buckingham, Chair
Professor William S. Hodgkiss, Co-Chair
Professor Florian Meyer

2022

The Thesis of Hong Jie Kok is approved, and it is acceptable in quality and form for publication on microfilm and electronically.

University of California San Diego

2022

TABLE OF CONTENTS

LIST OF FIGURES

LIST OF TABLES

ACKNOWLEDGEMENTS

I would like to acknowledge my thesis supervisor Professor Michael J. Buckingham for his support throughout the duration of the thesis. He provided invaluable insights into ocean acoustics and propagation, and he made the time to hold frequent meetings in person to discuss my progress on the thesis. His former doctoral student, Dieter A. Bevans, who authored the paper which this thesis is based upon, was also of immense help as he was present in many of these discussions. I am grateful to him for his assistance in providing the experimental data and in setting up the ocean propagation modelling tools.

I would also like to acknowledge the support that my organization, DSO National Laboratories, Singapore, have provided in terms of a scholarship that enabled me to complete my Masters of Science degree and carry out the work reported in this thesis.

ABSTRACT OF THE THESIS

Horizontal Coherence Function for Ambient Noise and Helicopter Sound in Water

by

Hong Jie Kok

Master of Science in Electrical Engineering (Applied Ocean Sciences)

University of California San Diego, 2022

Professor Michael J. Buckingham, Chair
Professor William S. Hodgkiss, Co-Chair

The radiated sound from an airborne source result in a head wave when it is incident on the sea bottom at the critical angle. The head wave travels along the sea bottom and exits at the same critical angle, and the pressure from the head wave can only be detected within a narrow range window due to geometrical spreading. Computing the horizontal coherence function from the data allows for the inference of the speed of sound in the sediment. The theoretical expression that was derived previously was validated in a new experiment that used

a line array with a wider aperture of 15 m as compared to a 3 m separation used in an earlier experiment. The least mean squares method was proposed for better estimation of the sediment sound speed instead of extracting the zero crossings when the data is noisy. Multiple ocean noise models were used for comparison with the coherence function computed for the ambient noise. The best fit for the ambient noise data consists of a convex combination of noise fields in order to account for the zero crossing locations and the amplitude of the coherence function at higher frequencies.

INTRODUCTION

The propagation of sound from an airborne source into an underwater medium has a major effect on the composition of the underwater sound field. One of the earliest studies was conducted by Urick, who evaluated the noise signature that was emitted by an overhead aircraft and recorded by an underwater hydrophone [1]. Medwin verified the predicted effect of the roughness of the air-water interface on the frequency components of the transmitted sound, where the resultant sound field depends on the relative positions of the source and the receiver in their respective mediums [2]. The entire setup can be modelled as a three-layer waveguide with a sea bottom sediment half-space representing the bottom most layer. Buckingham developed an analytical model that provided the solutions for both 2-D and a 3-D acoustic fields in each of the layers [3]. This opened up the possibility of exploiting the airborne source for various underwater acoustic applications, such as geo-acoustic inversion or determining the speed of a moving airborne source based on the changing Doppler frequencies as it passes through the closest point of approach [4]. Depending on the location of the receiver, the sound speed of the entire water column or the sound speed and attenuation characteristics of the sea sediment could be measured remotely. This may be more advantageous than deploying a temperature profiler in the case of the water column, or having to use a physical grabbing device to extract sediment samples for further analysis in a laboratory.

This thesis is primarily based on the publication "Estimating the sound speed of a shallow-water marine sediment from the head wave excited by a low-flying helicopter, 2017", and it involves geo-acoustic inversion using the head wave that is generated by an airborne source [5].

CHAPTER 1

Estimating the Sound Speed from the Head Wave

The publication [5] explores the use of a helicopter as a low-frequency sound source for underwater acoustics in shallow water regions. This chapter contains a summary of that work, which includes the problem definition, the theoretical background for the acoustic field solution, and the reported experimental results.

1.1 Problem Definition

As the helicopter hovers above the sea surface, the radiated sound is partially refracted into the ocean where some of the acoustic rays will interact with the sea bottom. Assuming that the speed of sound in the sediment is faster than the speed of sound in water, the head wave will be generated along the boundary between the underwater waveguide and the sea bottom as implied by Snell's law if the sound rays are incident at the critical angle.

The head wave propagates along the sea bottom at the speed of sound of the sediment and exits the sediment at the same critical angle. The pressure of the head wave is attenuated with range according to the inverse square law, which means that while the head wave may exit from more than one point along the sea bottom, there is a narrow range window where the majority of the measured pressure is contributed by the head wave. For a source that is far away, the pressure from the head wave decays proportionally to with the square of range and would have dissipated by the time it reaches the hydrophones. From the ray geometry, a source that is too near would result in most of the radiated energy not being incident on the sea bottom at the critical angle, and the head wave will exit the sea bottom at a range that is not detected by the array.

A hydrophone array that is positioned near the sea bottom within this range window is able to measure the outgoing head wave. The coherence function can be computed between a pair of hydrophones and compared with the theoretical expression that is derived for the head wave. It was observed that head wave was the major contributor to the acoustic field measured by the hydrophones when the helicopter is situated at the appropriate range and this allows for the inversion of the sediment sound speed.

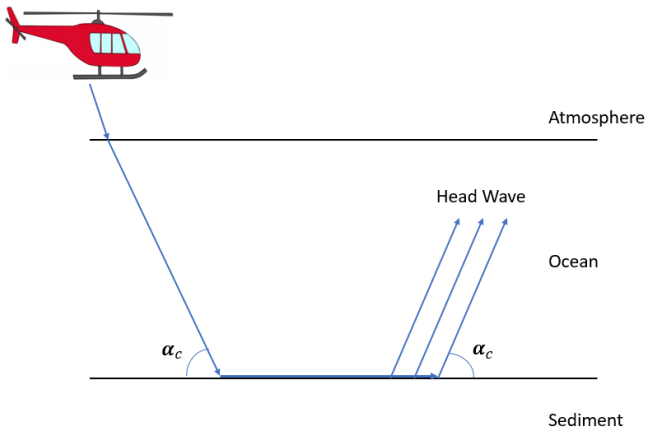

Figure 1: Illustration of the generation of the head wave from an airborne source at the critical angle.

1.2 Modelling the Three Layer Waveguide

The atmosphere, ocean channel and the sea bottom can be modelled together as a three-layer waveguide where each layer is treated as a homogenous fluid with a sound speed of c_j and a density of ρ_j where the subscript j refers to the respective layers. The velocity potential g_j for each layer can be represented as wave equations using the cylindrical coordinate system:

$$\frac{1}{r}\frac{\partial}{\partial r}\left(r\frac{\partial g_1}{\partial r}\right)+\frac{\partial^2 g_1}{\partial z^2}-\frac{1}{c_1^2}\frac{\partial^2 g_1}{\partial t^2}=\frac{S}{\pi r}\delta(r)\delta(z-z')\delta(t), \qquad z<0 \tag{1}$$

$$\frac{1}{r}\frac{\partial}{\partial r}\left(r\frac{\partial g_2}{\partial r}\right)+\frac{\partial^2 g_2}{\partial z^2}-\frac{1}{c_2^2}\frac{\partial^2 g_2}{\partial t^2}=0, \qquad 0\le z\le h \tag{2}$$

$$\frac{1}{r}\frac{\partial}{\partial r}\left(r\frac{\partial g_3}{\partial r}\right)+\frac{\partial^2 g_3}{\partial z^2}-\frac{1}{c_3^2}\frac{\partial^2 g_3}{\partial t^2}=0, \qquad z>h \tag{3}$$

where the z-axis is vertical and z is positive downwards from the origin, the source is represented by an impulse with an amplitude S, the depth of the water column is h and the airborne source is located at $r=r'=0$ and $z=z'<0$ above the sea surface as shown in Figure 2. The Helmholtz equations can be obtained by applying the Fourier transform to the previous three equations with respect to time to obtain G_j, which is the velocity potential in the frequency domain to obtain:

$$\frac{1}{r}\frac{\partial}{\partial r}\left(r\frac{\partial G_1}{\partial r}\right)+\frac{\partial^2 G_1}{\partial z^2}+k_1^2 G_1=\frac{S}{\pi r}\delta(r)\delta(z-z'), \qquad z<0 \tag{4}$$

$$\frac{1}{r}\frac{\partial}{\partial r}\left(r\frac{\partial G_2}{\partial r}\right)+\frac{\partial^2 G_2}{\partial z^2}+k_1^2 G_2=0, \qquad 0\le z\le h \tag{5}$$

$$\frac{1}{r}\frac{\partial}{\partial r}\left(r\frac{\partial G_3}{\partial r}\right)+\frac{\partial^2 G_3}{\partial z^2}+k_1^2 G_3=0, \qquad z>h \tag{6}$$

where $k_j=\frac{\omega}{c_j}$ is the acoustic wavenumber and ω is the angular frequency. The Hankel transform can be applied to the Helmholtz equations with respect to range:

$$G_{jp} = \int_0^\infty r G_j J_0(pr) dr$$

(7)

where $J_0(.)$ is the Bessel function of the first kind of order zero and G_{jp} is the velocity potential after the Hankel transform for the frequency domain velocity potential. The variable p simply denotes that the field is transformed. The inverse Hankel transform is given by:

$$G_j = \int_0^\infty p G_{jp} J_0(pr) dp$$

(8)

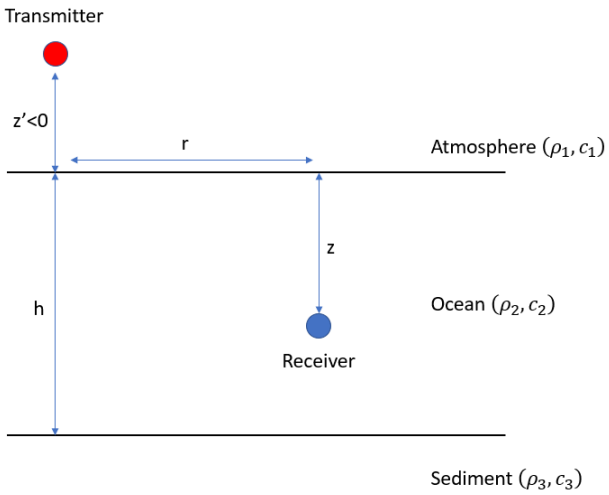

Figure 2: Depiction of the three-layer waveguide with the cylindrical coordinate system. The transmitter is positioned at a negative z coordinate.

Using the Hankel transform defined above, the Helmholtz equations are transformed into:

$$\frac{\partial^2 G_{1p}}{\partial z^2} + (k_1^2 - p^2) G_{1p} = \frac{S}{\pi} \delta(z - z'), \qquad z < 0$$

(9)

$$\frac{\partial^2 G_{2p}}{\partial z^2} + (k_2^2 - p^2) G_{2p} = 0, \qquad 0 \le z \le h$$

(10)

$$\frac{\partial^2 G_{3p}}{\partial z^2} + (k_3^2 - p^2)G_{3p} = 0, \qquad z > h$$

(11)

These equations are subjected to the boundary conditions of the continuity of pressure and the continuity of the normal component of particle velocity at both interfaces. By using the boundary conditions to solve for the unknown constants of the pressure field at each boundary, the transformed field for the ocean channel (the second layer) can be expressed as:

$$G_{2p}(z) = \frac{S}{\pi} e^{-i\eta_1|z'|} \left\{ \frac{\eta_1 cos[\eta_1(h-z)] + i\eta_1 b_{23} sin[\eta_2(h-z)]}{(\eta_2^2 + \eta_1\eta_3 b_{23} b_{21}) sin(\eta_2 h) - i\eta_2(b_{23}\eta_3 + b_{21}\eta_1) cos(\eta_2 h)} \right\}$$

(12)

where $b_{ji} = \frac{\rho_j}{\rho_i}$ and $\eta_j = \sqrt{k_j^2 - p^2}, Im(\eta_j) < 0$. By applying the inverse of the Hankel transform, the solution for the second layer becomes:

$$G_2(r, z; \omega)$$
$$= \frac{S}{\pi} \int_0^\infty p J_0(pr)\, dr e^{-i\eta_1|z'|} \left\{ \frac{\eta_1 cos[\eta_1(h-z)] + i\eta_1 b_{23} sin[\eta_2(h-z)]}{(\eta_2^2 + \eta_1\eta_3 b_{23} b_{21}) sin(\eta_2 h) - i\eta_2(b_{23}\eta_3 + b_{21}\eta_1) cos(\eta_2 h)} \right\} dp$$

(13)

This integral can be evaluated by expressing the Bessel function as a sum of Hankel functions of the first and second kind, and using contour integration in the complex p-plane to obtain a solution that consists of a sum of normal modes and three branch line integrals, where one of them corresponds to the head wave along the bottom boundary. This particular branch line integral can be written as:

$$I = \oint_{EJP} p H_0^{(2)}(pr) F(\eta_1, \eta_2, \eta_3)\, dp$$

(14)

where $H_0^{(2)}$ is the Hankel function of the second kind and zeroth order and

$$F(\eta_1,\eta_2,\eta_3) = e^{-i\eta_1|z'|}\left\{\frac{\eta_1 cos[\eta_1(h-z)] + i\eta_1 b_{23} sin[\eta_2(h-z)]}{(\eta_2^2 + \eta_1\eta_3 b_{23} b_{21})sin(\eta_2 h) - i\eta_2(b_{23}\eta_3 + b_{21}\eta_1)cos(\eta_2 h)}\right\}$$

(15)

The integration variable can be changed from p to η_3 as follows:

$$I = -\int_{-\infty}^{\infty} \eta_3 H_0^{(2)}\left(\sqrt{k_3^2 - \eta_3^2} r\right) F(\eta_1,\eta_2,\eta_3)\, d\eta_3$$

(16)

This integral can be evaluated using the method of modified stationary phase, and together with the assumption that horizontal range is far greater than the height of the water column h or the hydrophone depth, the head wave pressure expression can be simplified to:

$$I \approx \frac{b_{23} k_3}{r^2} e^{-[k_3 r + k_1|z'|sin(\beta_c)]}\left\{f_+ e^{i[k_2 r sin(\beta_c)]} + f_- e^{-i[k_2 r sin(\beta_c)]}\right\}$$

(17)

where

$$f_\pm = \frac{k_2 sin(\beta_c)}{L^2}[k_2 sin(\alpha_c) \pm b_{21} k_1 sin(\beta_c)]$$

(18)

$$L = k_2 sin(\alpha_c)\{k_2 sin(\alpha_c) sin[k_2 h sin(\alpha_c)] - i b_{21} k_1 sin(\beta_c) cos[k_2 h sin(\alpha_c)]\}$$

(19)

$$\alpha_c = cos^{-1}\left(\frac{c_2}{c_3}\right), \qquad \beta_c = cos^{-1}\left(\frac{c_1}{c_3}\right)$$

(20)

1.3 Coherence Function

Let a pair of underwater receivers be horizontally aligned with an airborne source, and they are situated at horizontal distances of r_1 and r_2 away from the source. The coherence function can be computed as:

$$\Gamma_{12} = \frac{\overline{I(r_1)I^*(r_2)}}{\sqrt{\left|\overline{I(r_1)}\right|^2 \left|\overline{I(r_2)}\right|^2}}$$

(21)

where $I(r_j) = I(r_j, z, |z'|; \omega)$ is the pressure due to the head wave measured by a hydrophone at range r_j, the overhead bar refers to the ensemble average and the asterisk represents the complex conjugate. When substituting Eq. (17) into Eq. (21), the horizontal coherence function can be simplified to:

$$\Gamma_{12} \approx exp[-ik_3(r_1 - r_2)]$$

(22)

It is implied in Eq. (22) that the real and imaginary components of the coherence function depend only on the separation between the two receivers and the speed of sound in the sediment. This presents the possibility of obtaining the sound speed of the sediment by computing the horizontal coherence function from the experimental data.

1.4 Experimental Setup

The authors of the publication conducted an experiment in 2016 to verify this theory. The site was located at a 16.5 m deep section near Scripps pier off the coast of Del Mar and a horizontal line array of hydrophones was mounted 0.5 m above the sea bottom. The array consists of eleven ITC 6050 hydrophones spaced out unevenly over a length of 12 m, however only two hydrophones with a separation of 2.97 m had sufficient signal to noise ratio to be used for analysis. Prior geological surveys by Scripps Institution of Oceanography indicate that the sediment at the site is mainly comprised of a 10 m thick layer of fine grain sand with an approximate sound speed of 1682 m/s. A Robinson R44 helicopter was used in the experiment that generates both broadband

noise and harmonics from its main and tail rotors. The tail rotor has a rotation rate that is six times that of the main rotor, which produces harmonics with a fundamental frequency of 81.6 Hz compared to 13.6 Hz for the main rotor. While the harmonics from the main rotor are visible only up to 100 Hz, the tail rotor harmonics can be observed up to 600 Hz. The higher frequencies are dominated by the broadband noise from the surface eddies that are generated by the rotors, until approximately 2.5 kHz where the radiated sound would have mostly dissipated.

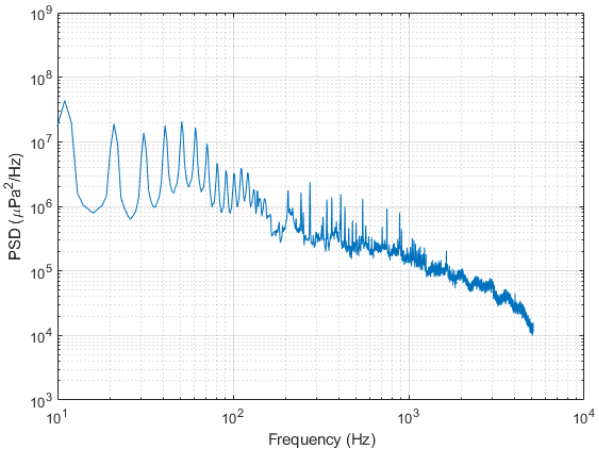

Figure 3: Power spectral density of the received signal on the hydrophone when the helicopter was at a range of 30 m.

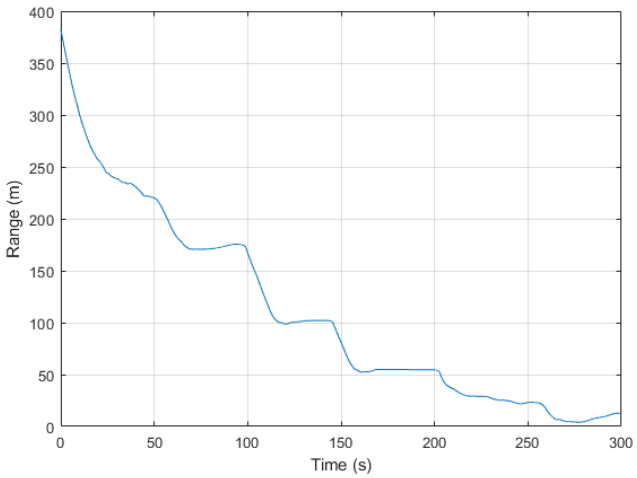

Figure 4: The trajectory of the helicopter. The helicopter hovered at various locations for 20 to 30 seconds each as it approached the end-fire of the array.

The helicopter approached the array from its end-fire. Starting at a distance of 300 m from the array, it hovered above the surface at various ranges from the first hydrophone with the rotors at a height of 4 m for a duration of 30 seconds. The coherence function was computed from the experimental data using Eq. (21) to estimate the value of c_3, which is the speed of sound in the sediment. This was done by obtaining the zeros from the real and imaginary components of the theoretical coherence function in Eq. (22) as follows:

$$c_3(n) = \frac{4f(n)R}{n} \tag{23}$$

where $R = |r_1 - r_2|$ and $f(n)$ is the frequency at which the n-th zero appears in the sine and cosine functions when taking in an argument of $n\pi/2$. The zeros are extracted by finding the minima of the magnitude of both the real and imaginary components of the coherence function that is computed from the data.

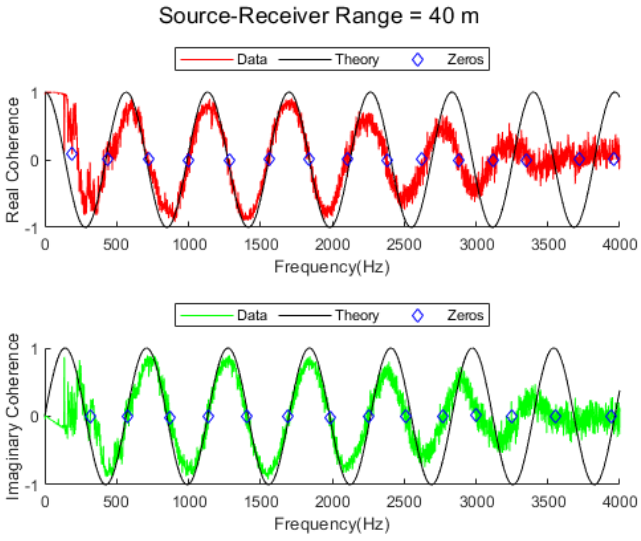

Figure 5: The horizontal coherence function is computed during a period where the helicopter was 40 m away from the first hydrophone. Computation was done with FFT length of one second with 50% overlap over 20 seconds of data.

Figure 5 shows the real and imaginary components of the horizontal coherence function that is computed when the helicopter was at a range of 40 m. At this position, a large amount of energy coming in at the critical angle to the sea bottom results in a dominant head wave. This is observed from the alignment of the coherence function from the data with the theoretical expression from Eq. (22) when a value of $c_3 = 1682$ m/s is used. The extracted zeros using the minima locating procedure are indicated in the figure, and the mean and the standard deviation of the values from Table 1 gives $c_3 = 1688.4 \pm 19.7$ m/s.

Table 1: Extracted zeros from the horizontal coherence function.

n	f(n) (Hz)	c_3 (m/s)
6	875	1732.5
7	1002	1700.5
8	1134	1684.0
9	1282	1692.2
10	1402	1665.6
11	1562	1687.0
12	1687	1670.1
13	1836	1677.8
14	1987	1686.1

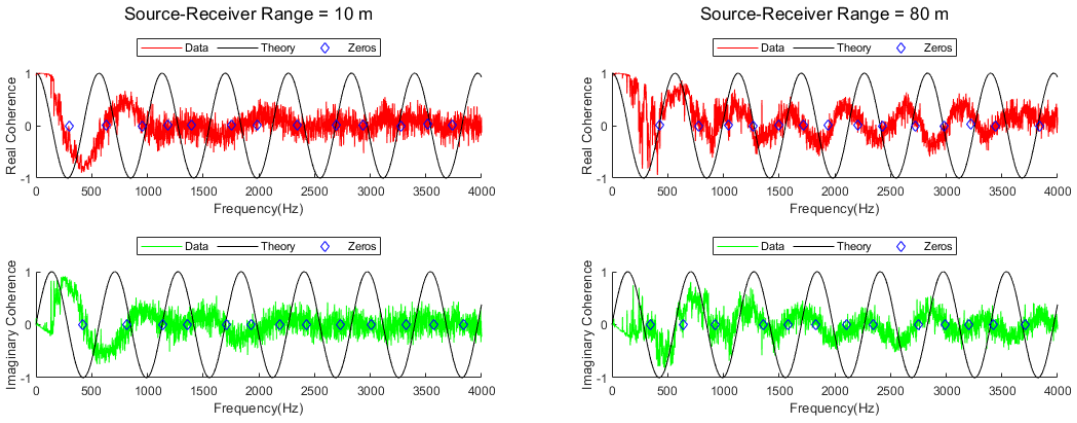

Figure 6: The horizontal coherence function is computed during a period where the helicopter was a) 10 m and b) 80 m away from the first hydrophone.

To support the argument that the head wave was observed only when the helicopter was at the right range, the authors also verified that the head wave was not present while the helicopter was either too near or too far from the array. Figure 6 shows the horizontal coherence plots for source ranges of 10 m and 80 m where the theoretical curves are poorly matched to the data. In the case of 80 m, the helicopter would have been too far away and the generated head wave would have dissipated before it reaches the array. The observed coherence function in this case is solely due to the ambient noise, which will be discussed in further detail in CHAPTER 3. When the helicopter is 10 m away from the array, most of the radiated sound will be incident on the array at an angle that is greater than the critical angle, resulting in most of the measured pressure to come from refracted waves that travel through the water column. As the sound speed of water is lower than that of the sediment, the resulting coherence function has zero crossings that are further out in frequency than the theoretical curve derived for the sediment. Hence the head wave is indeed observable only within a narrow source-range window.

CHAPTER 2

Analysis of the 2019 Dataset

In 2019, the authors of the publication [5] returned to the same location to conduct a second experiment, this time using a longer hydrophone array with four hydrophones. The hydrophone layout is shown in Figure 7 and it is noted that hydrophones 3 and 4 have almost the same separation as the pair of hydrophones that was used for analysis in the previous chapter. The array was mounted at the same depth as before and the composition of the sea sediment remains the same. This chapter contains the thesis author's analysis of the horizontal coherence function that was computed for all six pairs of hydrophones.

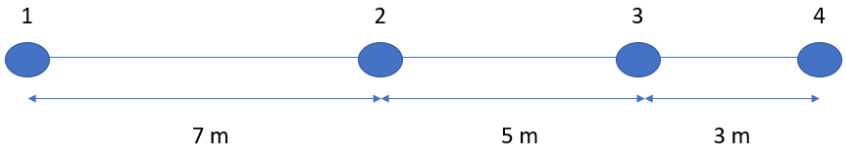

Figure 7: Hydrophone array spacings for the 2019 experiment. The array has a total length of 15 m with the widest spacing at 7 m.

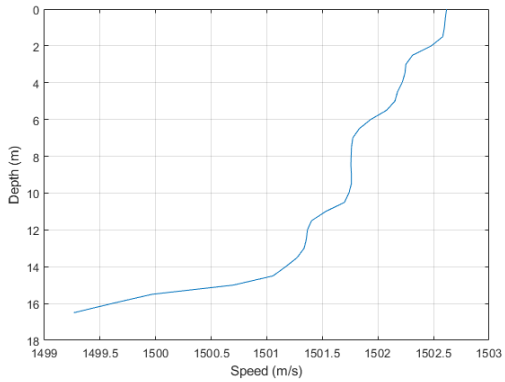

Figure 8: Sound speed profile from the experiment site in 2019. The temperature profile was collected and a salinity of 33.5 psu (historical average) was used for the computation.

2.1 Coherence Function from the 2019 Dataset

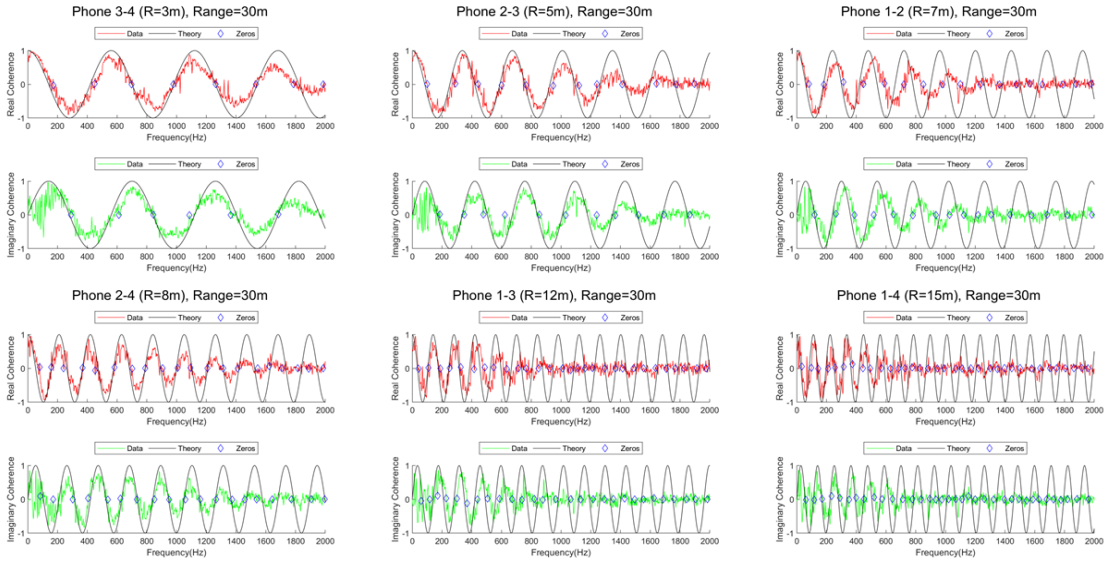

Figure 9: Coherence function plotted against frequency for all hydrophone pairs when helicopter is 30 m away from the first hydrophone.

Figure 9 shows the coherence curves plotted against frequency with the estimated zeros. It is observed that the coherence function vanishes at higher frequencies with increasing spacing between the hydrophones, with a higher limit of 600 Hz for a separation of 15 m. This is due to the higher attenuation for higher frequencies where the amplitude of the coherence function decays much faster with geometric spreading. As the coherence function for the head wave is a function of sensor separation and sediment sound speed, it would be easier to verify the consistency of the coherence function by plotting against a normalized frequency axis of $\omega d/c$.

Figure 10 and Figure 11 show the coherence function when plotted against normalized frequency for various hydrophone pairs when the helicopter is at a range of 10 m and 30 m away from the first phone. It is observed in both figures that the coherence function curves for all the hydrophone pairs are similar in shape for the respective time instances at which they were measured.

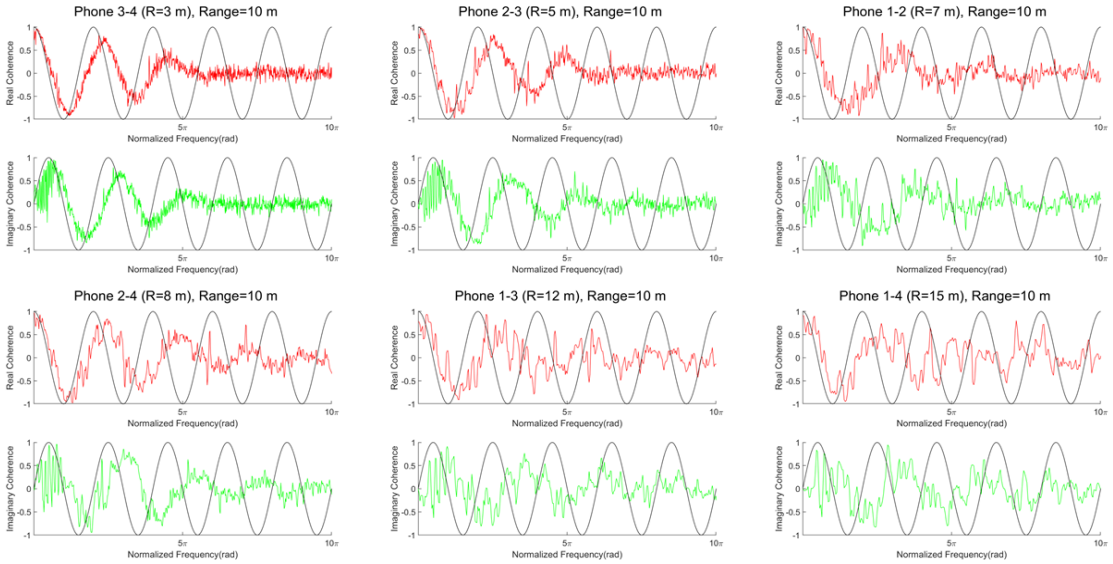

Figure 10: Coherence function plotted against normalized frequency for all hydrophone pairs when helicopter is 10 m away from the first hydrophone.

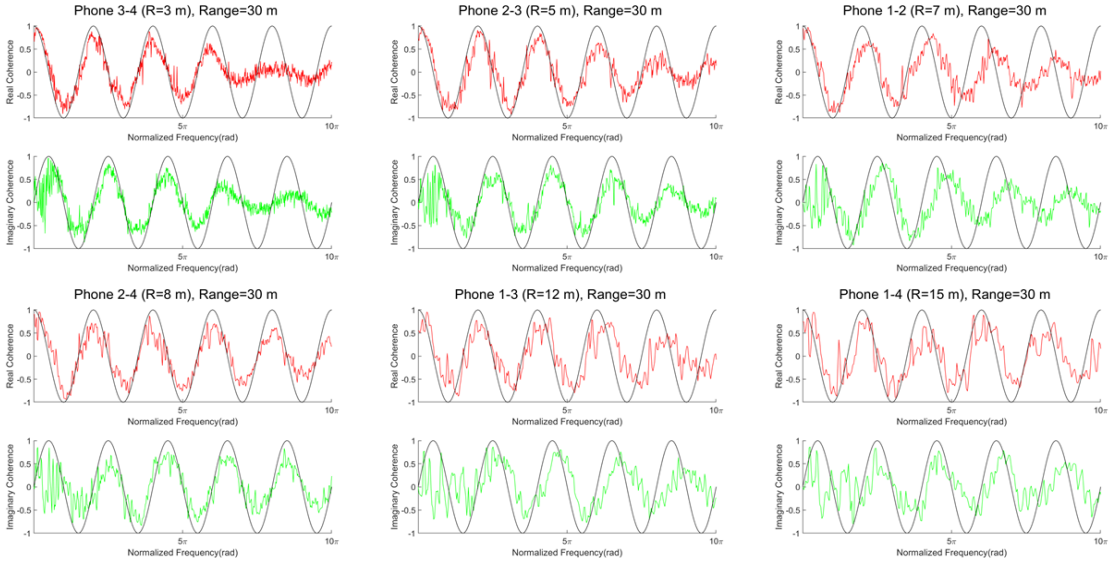

Figure 11: Coherence function plotted against normalized frequency for all hydrophone pairs when helicopter is 30 m away from the first hydrophone.

Figure 10 shows a clear mismatch between the theoretical coherence function and the data which is to be expected as the helicopter was not at the right range. Figure 11 shows a good agreement between the curves for all hydrophone pairs, which validates Eq. (22) by showing that

it works for various hydrophone spacings at least up to 15 m assuming that the helicopter lies within the right range window. The coherence function appears to vanish at a normalized frequency of 7π for a separation of 3 m and this takes place at approximately 1800 Hz, which is slightly lower than what was observed in the 2016 experiment.

2.2 Estimating Sediment Sound Speed

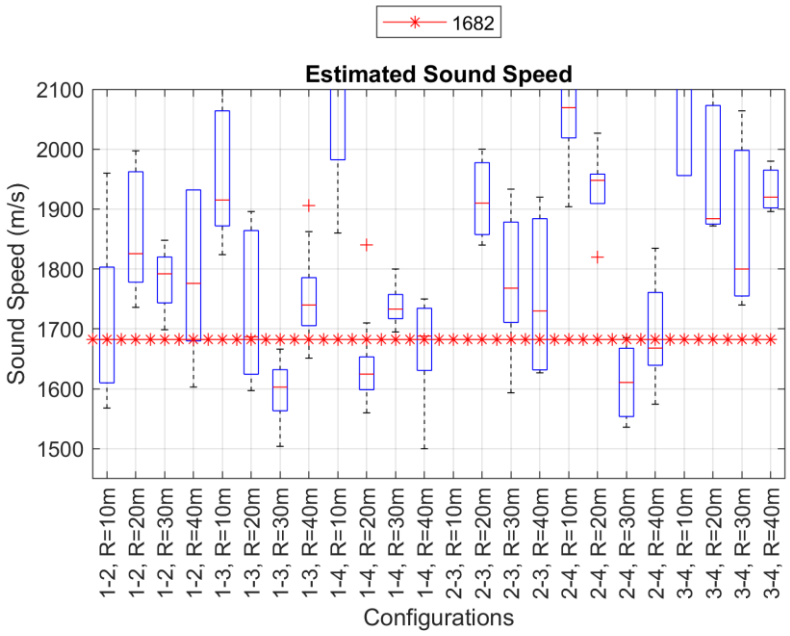

Figure 12: Box plot of the sound speeds that are obtained for each configuration. The mean and variance are computed using the zeros that reside between 150 to 500 Hz.

Figure 12 shows the statistics for each configuration in a MATLAB box plot for the estimated sound speeds from the zeroes between 150 to 500 Hz where the coherence function was still observable for all spacings. The top and bottom of the blue box are the 75^{th} and 25^{th} percentile of the zero crossings, the red dash in the blue box is the mean, while the top and bottom black edges extending from the boxes are the maximum and minimum for the zero crossings. The horizontal line marked by red asterisks refer to the ground truth sediment sound of 1682 m/s. It is

expected that only the R=30 m and R=40 m configurations will be centered around the ground truth sediment speed of 1682 m/s. The data only shows good agreement for the hydrophone combinations 1-4 and 2-4 for R=40 m, with 1-2 and R=10 m being unusually close to the ground truth considering that the head wave should not be detected at that range. It is noted that the coherence function curves are generally noisier than the ones obtained in 2016. This may be caused by the shorter duration of time the helicopter spent hovering above each position, which in turn reduces the time period where the coherence function will remain stable. The noisier curves result in a poor estimation of the zeros and inaccurate sound speed computations with Eq. (23).

An alternative way of estimating the sound speed is to apply least squares fitting of the coherence curves from the data to a set of theoretical coherence curves that are obtained by substituting a range of sediment sound speeds into Eq. (22). This provides an intuitive approach where the entire shape of the coherence curve is matched, rather than just obtaining the position of the zero crossings which can be heavily influenced by the noise. The theoretical coherence is computed for every hydrophone pair as such:

$$\Gamma_c = exp\left[-i\frac{\omega}{c}(r_1 - r_2)\right] \tag{24}$$

The estimated sound speed is given by:

$$c^* = \min_c mean\left(Re(\Gamma_c) - Re(\Gamma_{data})\right)^2 + mean\left(Im(\Gamma_c) - Im(\Gamma_{data})\right)^2 \tag{25}$$

Where Γ_{data} is the coherence function computed from the data. The estimated sound speed c^* minimizes the mean difference between both the real and imaginary components of the coherence function from the data and the theoretical curve. Due to the attenuation at higher frequencies, the frequency range used for comparison is limited from 100 to 550 Hz, which is different from the

800 – 2000 Hz band that was used for extracting zeroes in the 2016 experiment. Figure *13* and Figure *14* show examples of the best fit curve from the least squares method lined up against the data and the theoretical curves when the helicopter is at a range of 30 m and the x-axis is frequency and normalized frequency respectively. The results are shown in Figure 15, where there is a distinct pattern of increasing accuracy for each hydrophone pair as the helicopter approached the range of 30 m, with the only exception being hydrophone pair 3-4 that provided a higher sound speed. This can be rectified by adjusting the least square fit to a normalized frequency range of 0 to 6π radians and the results are shown in Figure 16. The trend becomes clearer for hydrophone pairs with a smaller separation such as 2-3 and 3-4 where the estimated sound speed matches the ground truth quite well. The least squares fit has shown to be a more suitable approach to estimating the sediment sound speed from the coherence function especially for hydrophone pairs with a higher separation.

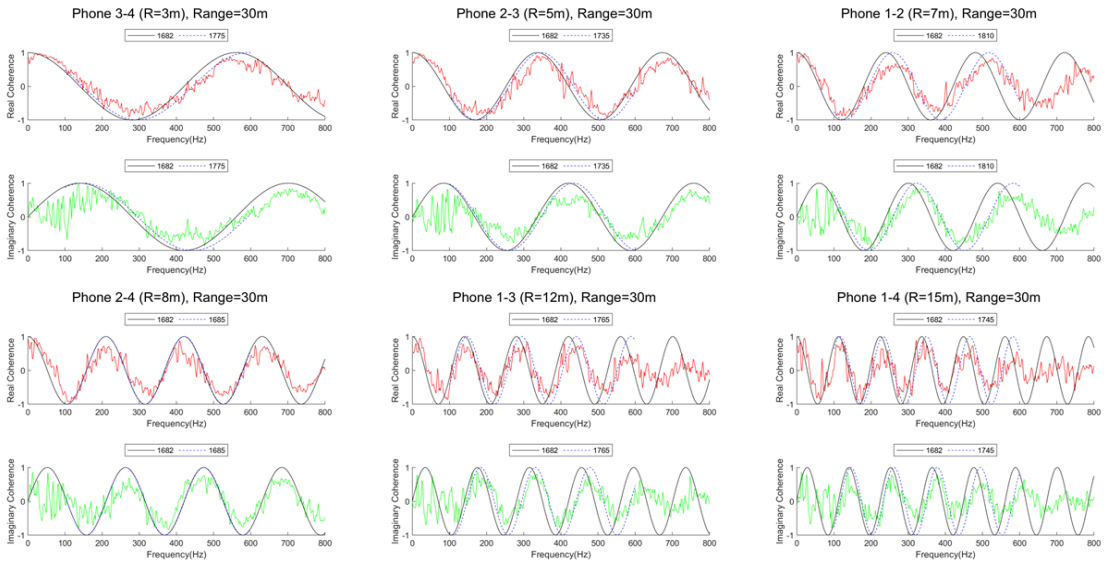

Figure 13: Best least square fit against frequency for the 2019 dataset when the helicopter is at a range of 30 m from the first hydrophone.

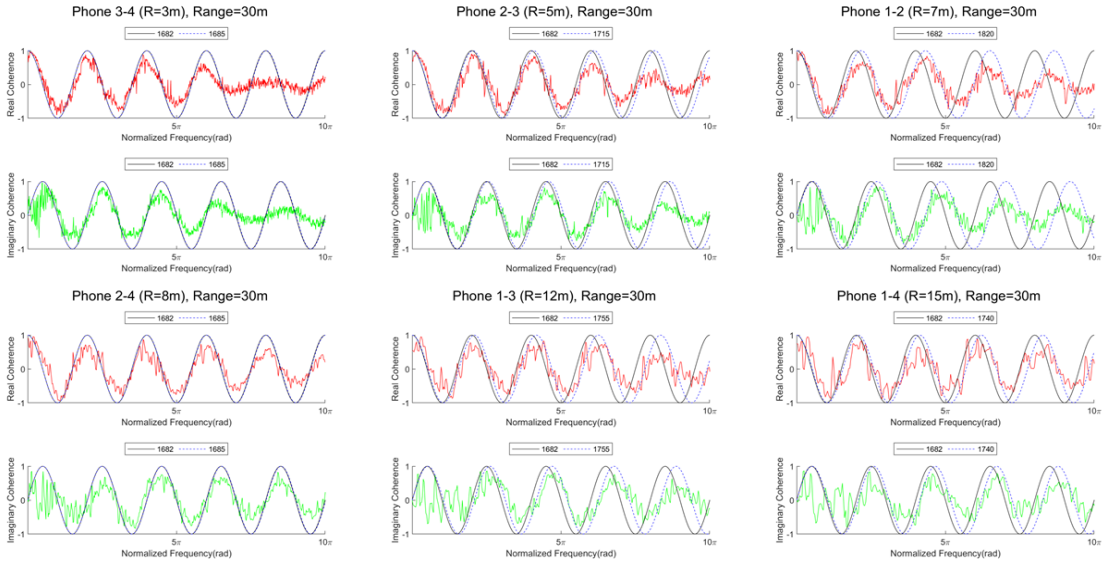

Figure 14: Best least square fit against normalized frequency for the 2019 dataset when the helicopter is at a range of 30 m from the first hydrophone.

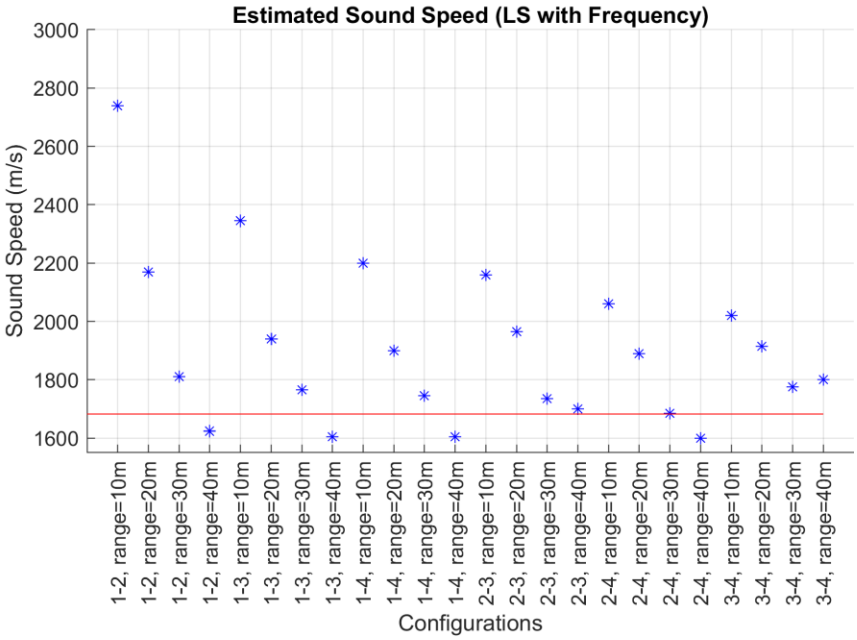

Figure 15: Best estimated sound speeds from least square fit against frequency for the 2019 dataset.

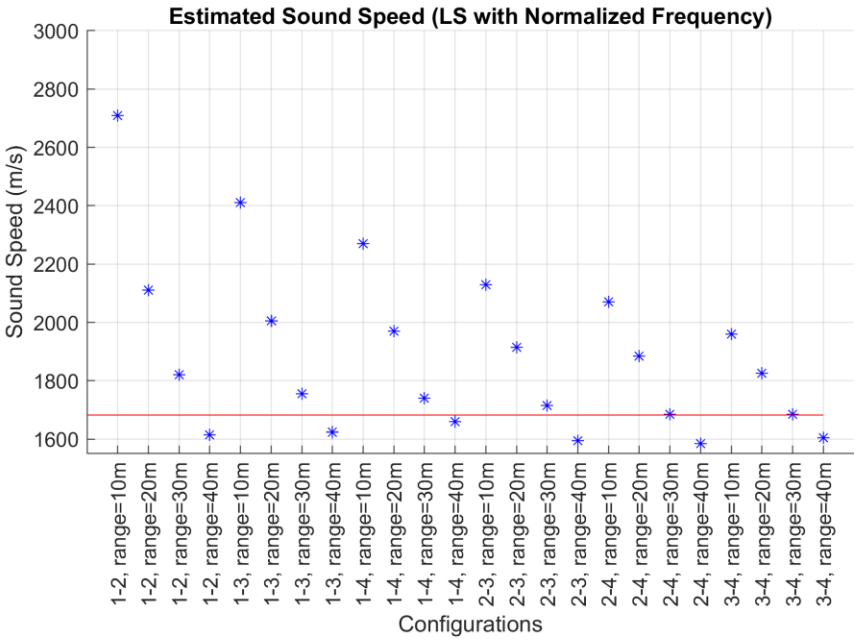

Figure 16: Best estimated sound speeds from least square fit against normalized frequency for the 2019 dataset.

2.3 SCOOTER Simulation

SCOOTER is a Fast Field Program (FFP) that evaluates spectral integral directly with the range independent assumption, where FFP models compute the contour integration of an acoustic pressure representation and includes the near field contributions which might be neglected by normal mode computations [6]. SCOOTER was used to simulate the pressure fields that are observed at all hydrophones based on the experimental setup in 2019. Figure 17 to Figure 19 shows the SCOOTER simulated coherence curves with the experimental data when plotted against normalized frequency. The SCOOTER output appears to be mismatched to the data when the source was 10 m away in Figure 17, with the largest discrepancy being observed for hydrophones 3 and 4 where the second to the fourth zero crossings are overestimated by SCOOTER. This means that the SCOOTER simulation generated more air to water refracted wave arrivals than the actual wave propagation during the data collection.

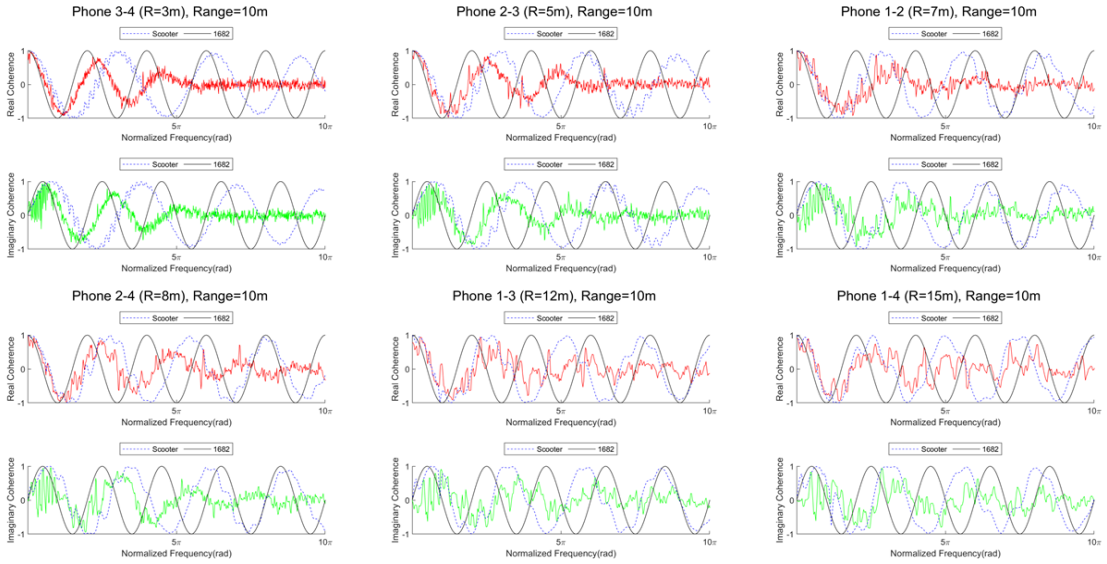

Figure 17: SCOOTER simulation compared with the theoretical curves and the experimental data against a normalized frequency axis with the source being 10 m away from the first phone.

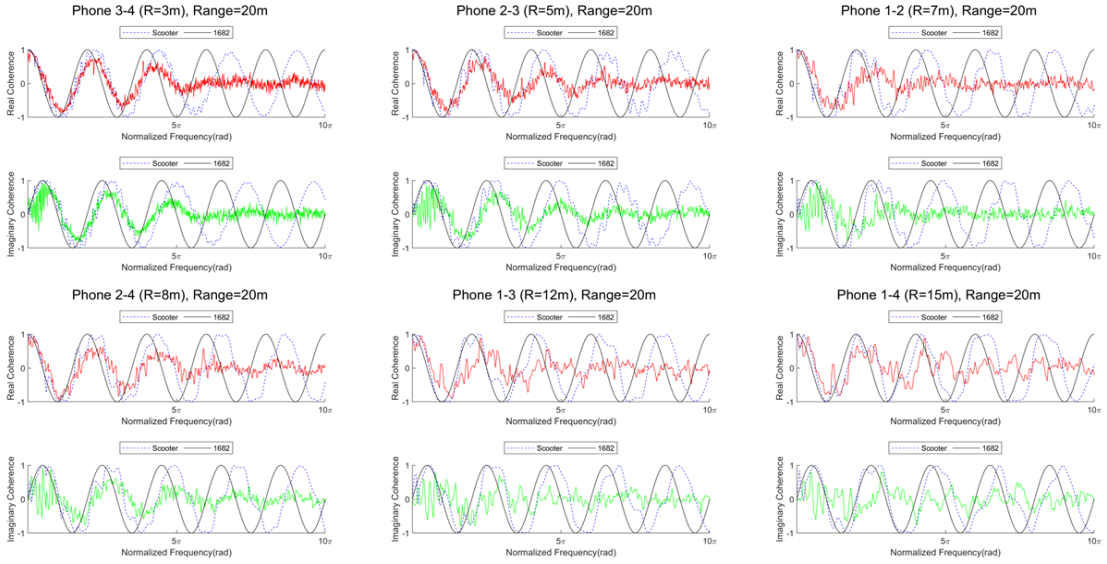

Figure 18: SCOOTER simulation compared with the theoretical curves and the experimental data against a normalized frequency axis with the source being 20 m away from the first phone.

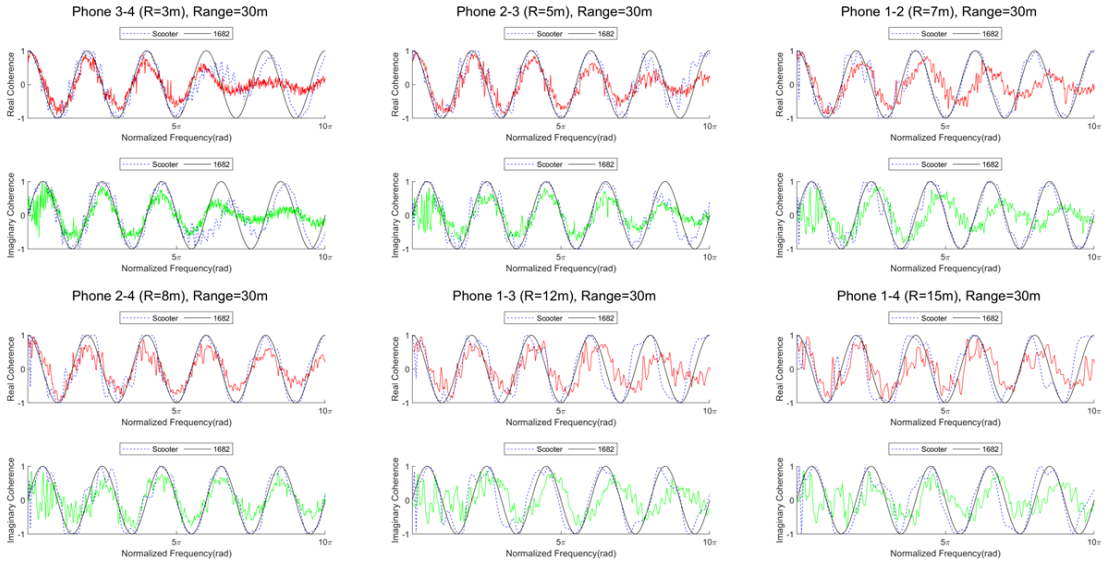

Figure 19: SCOOTER simulation compared with the theoretical curves and the experimental data against a normalized frequency axis with the source being 30 m away from the first phone.

The SCOOTER output aligns well with the data at least up to the first four zero crossings when the source was 20 m and 30 m away, at least for the lower normalized frequency range where the signal to noise ratio was sufficiently high. Figure 19 shows the coherence curves for when the helicopter is situated at the right range for generating the head wave, and the theoretical curves line up with both the SCOOTER output and the data for all hydrophone pairs which further validates Eq. (22).

CHAPTER 3

Ambient Noise Analysis

This chapter examines the coherence function when ambient noise is present. The work presented in this chapter consists of the expressions derived for various ocean ambient noise models and they are compared to the coherence function formed from the hydrophone pairs during a time period that was prior to the arrival of the helicopter. The aim is to determine the best model fit for the ambient noise observed during the experiment. While the wind speed was not measured during the experiment, it was noted from recorded videos that the conditions were relatively calm and the surface noise should not be significant. To simplify the modelling, the discussion will begin with basic models that assume that reflections off the sea floor are negligible despite the shallow water environment used for the experiment.

3.1 Volume and Surface Noise Model

Cron and Sherman presented a model for ocean noise as a combination of an isotropic noise field and a directional noise field on the surface [7]. The isotropic noise model or the volume noise model assumes that there are multiple noise sources that are uniformly distributed in a sphere of a certain radius. For a homogenous field, the pressure measured by the receivers can be given as:

$$\langle e^2 \rangle_2 = 2\langle e^2 \rangle_1 [1 + \rho(\boldsymbol{X}_1, \boldsymbol{X}_2, \tau_{12})] \tag{26}$$

$\langle e^2 \rangle_1$ and $\langle e^2 \rangle_2$ are the mean-square outputs of one receiver and both receivers respectively while $\rho(\boldsymbol{X}_1, \boldsymbol{X}_2, \tau_{12})$ is the normalized spatial correlation function for the pressure at positions $\boldsymbol{X}_1$ and

$\boldsymbol{X}_2$ with τ_{12} as the time delay. For a single receiver located at the center of a sphere of radius R_v that is filled with noise sources, the output from one frequency is given by:

$$e_1 = (A/ikr)e^{i(kr-\omega t+\delta)} \tag{27}$$

where r is the distance between the noise source and the sensor, k is the wavenumber and A and δ are constants. The real part of this output can be squared and averaged over time, and by assuming random phase contributions from all sources within that sphere, the mean square output of one receiver can be obtained:

$$\langle e^2 \rangle_1 = 2\pi \langle A^2 \rangle R_v / k^2 \tag{28}$$

where $\langle A^2 \rangle$ is the time average of A^2. By placing the midpoint of two sensors at the center of the sphere, the spatial correlation function now depends on the distance $d = 2r_0$ between the two receivers where r_0 is the distance from one phone to the midpoint. At the same time the sum of the outputs of the two receivers due to a single noise source can be given by:

$$e_1 + e_2 = \begin{cases} 2Ae^{-i(\omega t-\delta)} \sum_{n\,even} (2n+1) {h_n}^{(1)}(kr_0) j_n(kr) P_n(cos\theta) & (r \le r_0) \\ 2Ae^{-i(\omega t-\delta)} \sum_{n\,even} (2n+1) j_n(kr_0) {h_n}^{(1)}(kr) P_n(cos\theta) & (r \ge r_0) \end{cases} \tag{29}$$

Where ${h_n}^{(1)}$ is the spherical Hankel function of the first kind of the n-th order, $P_n(cos\theta)$ is the Legendre polynomial, and j_n is the spherical Bessel function of the n-th order. $\langle e^2 \rangle_2$ can be obtained by taking the taking the square and the time average of the real part of Eq. (29), then integrating it over the volume of the same sphere. By setting $R_v \to \infty$ for the volume noise model, the spatial correlation function $\rho(d, \gamma)$ for a pair of horizontally aligned sensors with $\gamma = 0$ being the angle between the line joining the receivers and the surface is given by:

$$\rho(d,0) \to 2\sum_{n\,even}(2n+1){j_n}^2(kr_0) - 1 = \frac{\sin kd}{kd}$$

(30)

which is an established result in literature for isotropic noise. The second component of the noise field, which is also known as the surface noise model, assumes that there are noise sources uniformly distributed over a circular radius R_s on the surface. An additional assumption of having the distance between the receivers and the surface being much greater than the distance between the receivers is needed to perform the evaluation. By first evaluating the mean square outputs as done previously for the volume noise model, the spatial correlation function can be obtained as:

$$\rho(d,\gamma) = \frac{\int_0^{\frac{\pi}{2}} g^2(\alpha)\ tan\alpha\ cos(kd\ sin\gamma\ cos\alpha)\ J_0(kd\ cos\gamma\ sin\alpha)\ d\alpha}{\int_0^{\frac{\pi}{2}} g^2(\alpha)\ tan\alpha\ d\alpha}$$

(31)

where α is the grazing angle from the surface noise source to the receiver and $g(\alpha)$ is the directionality function of each surface noise source. When each source is assumed to be omni-directional with $g(\alpha) = 1$, the function is simplified as:

$$\rho(d,\gamma) = J_0(kd\ cos\gamma)$$

(32)

Figure 20 and Figure 21 show the coherence function plots at different timings during the data collection with both the volume and surface noise models when the helicopter was absent. The amplitudes for the theoretical expressions decay noticeably with higher frequency especially for the volume noise model. The amplitude for the experimental data remains high at the higher frequencies which suggests that there are other sources of coherence.

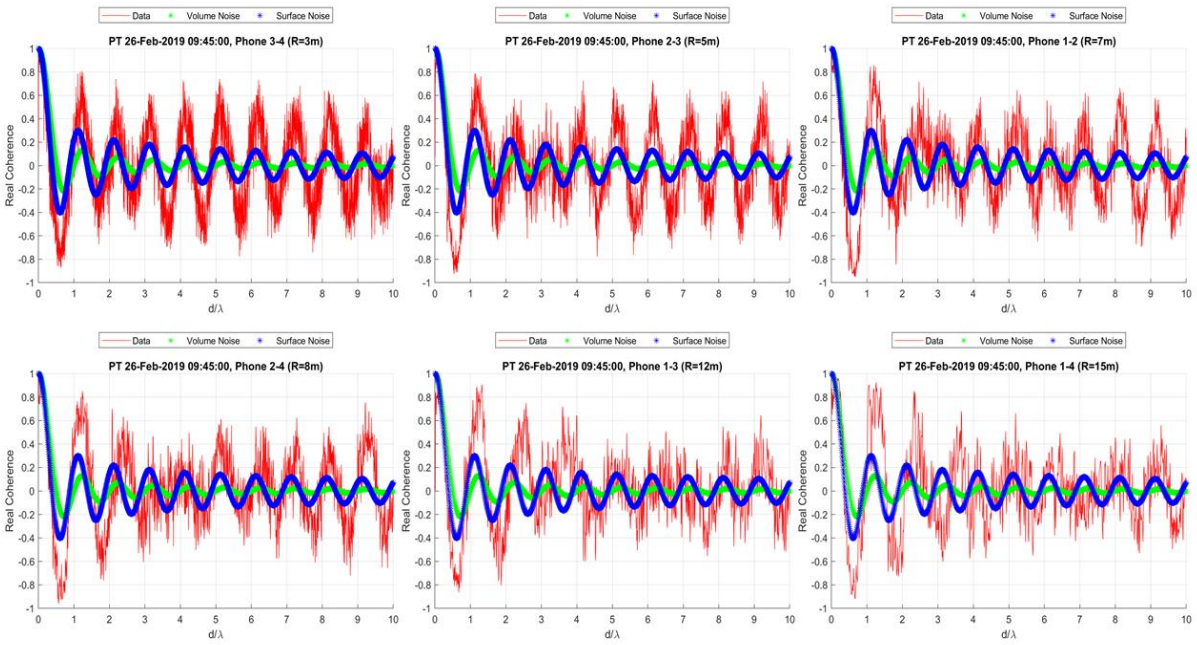

Figure 20: Coherence function plots for the data at 09:45 PT. The green and blue curves correspond to the volume and surface noise models respectively.

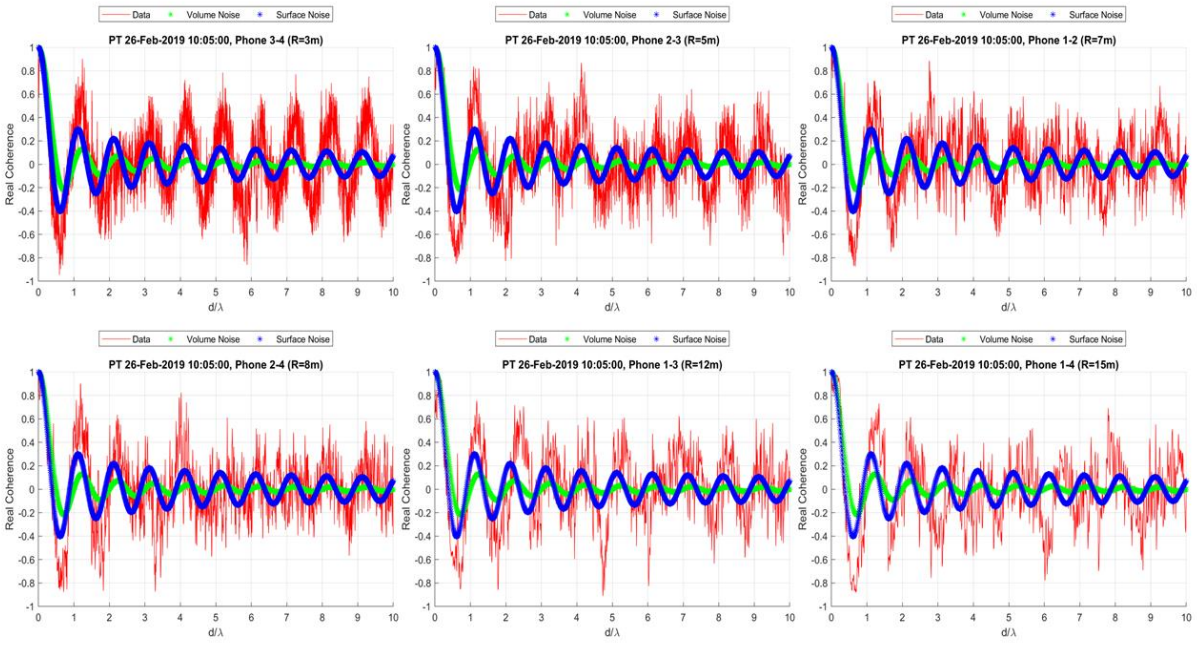

Figure 21: Coherence function plots for the data at 10:05 PT. The green and blue curves correspond to the volume and surface noise models respectively.

In both cases, the zero crossings for the volume noise model appears to be slightly more aligned with the data at least for hydrophone separations of up to 8 m, which suggests that the

noise field is primarily isotropic at those spacings. This may be surprising considering that the depth of the receivers is only 16 m and hence it was assumed that the surface noise model would provide a better match. There is a mismatch between the data and the theoretical expressions beyond the third zero crossing for the last two hydrophone spacings of 12 m and 15 m. This is expected as the distance between the receivers are more than half the depth, and the assumptions needed for Eq. (31) will not hold.

3.2 Numerical Modelling with OASES

Given that neither the volume noise model nor the surface noise model can account for the higher coherence at higher frequencies, numerical modelling for ambient noise was performed with OASES, which models the acoustic propagation in horizontally stratified waveguides using wavenumber integration [8]. OASES requires the input of the water column depth, the position of the sensors and the sea floor properties to generate an ambient noise field that takes into account the noise reflections from the bottom. There is a sub-module within the program package that models the propagation of surface-generated ambient noise and provides the sensor response.

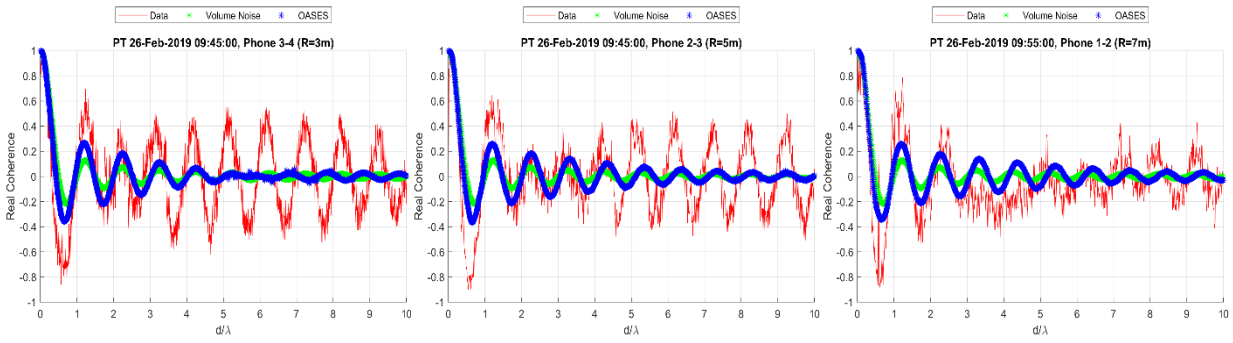

Figure 22: Comparison of the volume noise model, the OASES output and the experimental data at 9:45 PT.

It is observed in Figure 22 that the volume noise model was still a better match to the data than the OASES output in terms of zero crossings at the higher frequencies. Given that OASES is producing more reflected wave arrivals from the bottom, the zero crossings are pushed further out than what is shown by the data. Based on the above results, the sea bottom might not be contributing significantly to the ambient noise field.

All three models explored thus far were not able to adequately describe the coherence function for the ambient noise. This provides the motivation to use a generalized expression that accounts for multiple noise fields to fit the ambient noise that was observed during the experiment

3.3 Generalized Spatial Correlation

Cox developed expressions for the normalized cross spectral density between a pair of hydrophones when they are in a noise field with an arbitrary directional distribution of uncorrelated plane waves [9]. For a three-dimensional field, the normalized directional density function $F(\theta, \phi, \omega)$ is given by:

$$\frac{1}{4\pi}\int_0^{2\pi}\int_0^{\pi} F(\theta,\phi,\omega)sin\theta d\theta\, d\phi = 1 \tag{33}$$

Where θ is the elevation and ϕ the azimuth. For the special case of azimuthally uniform fields, the normalized directional density function can be simplified by integrating over ϕ to give:

$$\frac{1}{2}\int_0^{2\pi} F(\theta,\omega)sin\theta d\theta = 1 \tag{34}$$

The normalized cross spectral density is given by:

$$\rho(d,\omega;\gamma,\zeta) = \frac{1}{4\pi}\int_0^{2\pi}\int_0^{\pi} F(\theta,\phi,\omega)\, sin\theta \exp\{i(\omega d/c)[sin\theta sin\gamma cos(\phi-\zeta) + cos\theta cos\gamma]\}\, d\theta\, d\phi \tag{35}$$

Where d is the sensor separation, γ is the angle between the line joining both sensors and the surface in terms of elevation and ζ is the same angle for azimuth. Assuming an azimuthally uniform field allows for Eq. (35) to be rewritten as:

$$\rho(d,\omega;\gamma,\zeta) = \frac{1}{2}\int_0^{\pi}\left[\frac{1}{2\pi}\int_0^{2\pi} \exp\left\{i\left(\frac{\omega d}{c}\right)\,[sin\theta sin\gamma cos(\phi-\zeta)]\right\} d\phi\right] F(\theta,\omega)\, sin\theta \exp\{i(\omega d/c)cos\theta cos\gamma\}\; d\theta \tag{36}$$

The inner integral can be evaluated as a Bessel function which gives:

$$\rho(d,\omega;\gamma) = \frac{1}{2}\int_0^{\pi} J_0\left[\left(\frac{\omega d}{c}\right) sin\theta sin\gamma\right] F(\theta,\omega)\, sin\theta \exp\{i(\omega d/c)cos\theta cos\gamma\}\; d\theta \tag{37}$$

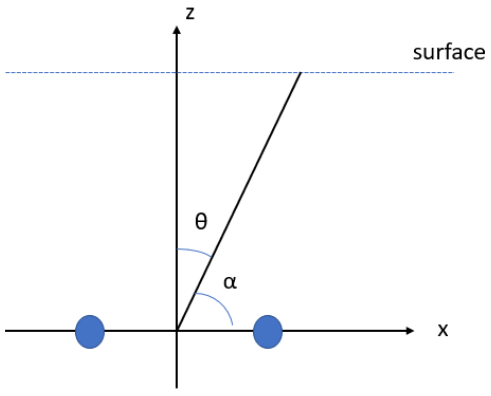

Figure 23: Illustration of the grazing angle α in relation to the angle θ that is used in the equations above. The line joining the receivers are parallel to the surface and ocean floor.

It is now possible to examine the contribution to the coherence function from the ambient noise that is coming from within a grazing angle of $\pm\beta°$. Let $F(\theta,\omega)$ be rewritten using a change of variable from θ to α:

$$F(\alpha,\omega)=\begin{cases}F_0 & \alpha\leq\beta,\alpha\geq-\beta\\ 0 & \alpha>\beta,\alpha<-\beta\end{cases}$$

(38)

Where F_0 is a constant. The normalized density function in Eq. (34) can be rewritten using $\alpha=\frac{\pi}{2}-\theta$ based on Figure *23* as shown below:

$$\frac{1}{2}\int_{-\beta}^{\beta}F_0 cos\alpha=1$$

(39)

Solving Eq. (39) gives $F_0=\frac{1}{sin\beta}$. By substituting F_0 back into Eq. (37) and setting $\gamma=0$, the coherence function for vertically aligned sensors can be written as:

$$\rho(d,\omega;0)=\frac{1}{2sin\beta}\int_{-\beta}^{\beta}cos\alpha\exp\{i(\omega d/c)sin\alpha\}\,d\alpha=\frac{sin[(\omega d/c)sin\beta]}{(\omega d/c)sin\beta}$$

(40)

Setting $\gamma=\frac{\pi}{2}$ gives the result for horizontally aligned sensors:

$$\rho\left(d,\omega;\frac{\pi}{2}\right)=\frac{1}{2sin\beta}\int_{-\beta}^{\beta}J_0\left[\left(\frac{\omega d}{c}\right)cos\alpha\right]cos\alpha\,d\alpha$$

(41)

There is no closed form solution to Eq. (41) hence the whole expression has to be evaluated in MATLAB for a given value of β.

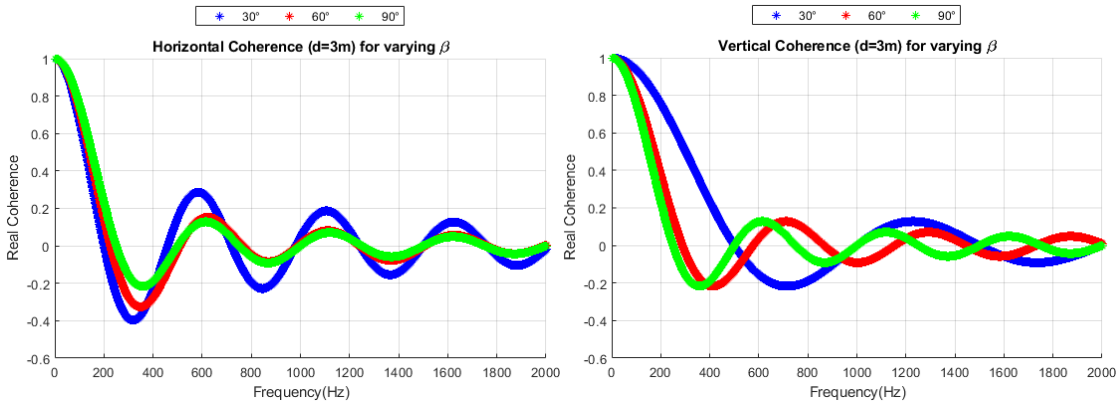

Figure 24: Plots for the coherence function for a pair of horizontally and vertically aligned sensors for different angles of β.

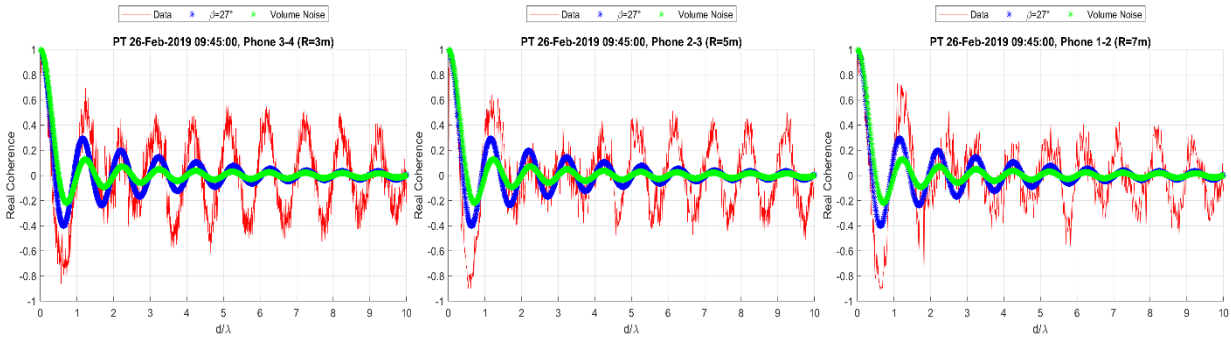

Figure 25: Comparison of the volume noise model, the generalized horizontal coherence function for $\beta = 27°$ and the experimental data at 09:45 PT.

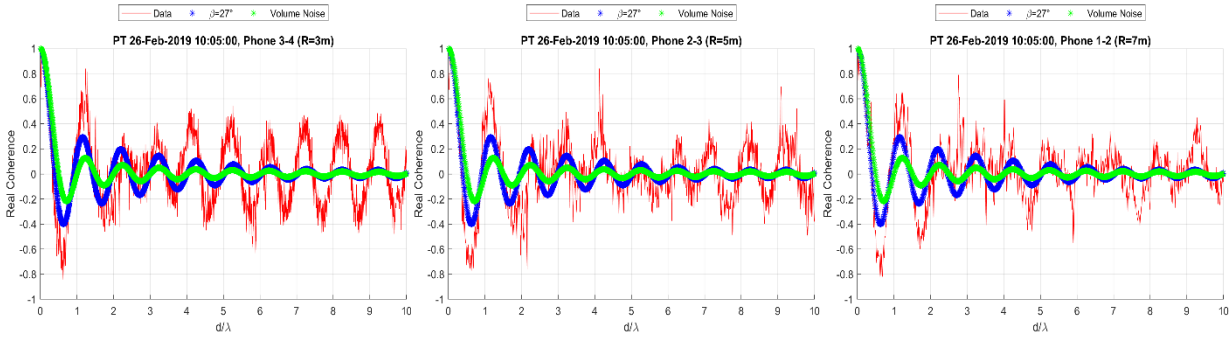

Figure 26: Comparison of the volume noise model, the generalized horizontal coherence function for $\beta = 27°$ and the experimental data at 10:05 PT.

Figure 24 shows the coherence functions for cases where the sensors are either horizontally or vertically aligned by setting β to various angles. As a sanity check, it is noted that $\beta = 90°$ for both alignments leads to the isotropic noise model which is expressed as $\frac{\sin kd}{kd}$.

The critical angle was determined to be 27° based on the ground truth sediment speed of 1682 m/s. Figure 25 and Figure 26 show the plots of the coherence function for the ambient noise measured on two different occasions by comparing the volume noise model with the generalized horizontal coherence function by assuming that the ambient noise is restricted to a sector of $\pm 27°$ which is within the critical angle. The first zero crossing of the generalized coherence function appears to be more aligned with the data than the volume noise model, but both models match the data quite well at higher frequencies.

To account for the higher amplitude for the coherence function, it is likely that there is an additional directional component in the noise field. Cox addressed the issue of overlapping noise fields in his paper by proposing that they can be represented by a convex combination of an isotropic and a directional component:

$$X(\phi, \omega) = Y(\omega) + [1 - Y(\omega)]D(\phi, \omega) \tag{42}$$

where $0 \leq Y(\omega) \leq 1$ and $D(\phi, \omega) \geq 0$, and $D(\phi, \omega)$ is a normalized directional density function. Given that the hydrophone array was positioned near the shore, it is possible that there could be waves that contribute to the amplitude of the coherence function as an additional sinusoidal component. This noise component is modelled as a field that is incident on the array at only one elevation and one azimuth and it can be expressed as:

$$F_2(\alpha, \phi, \omega) = \begin{cases} F_2(\alpha, \omega) & \phi = \phi_1 \\ 0 & \phi \neq \phi_1 \end{cases} \tag{43}$$

$$F_2(\alpha,\omega) = \begin{cases} G & \alpha = \alpha_1 \\ 0 & \alpha \neq \alpha_1 \end{cases}$$

(44)

where ϕ_1 and α_1 are the azimuth and elevation angles from which the waves are coming from and G is a constant to be determined. Substituting the definition of $F_2(\alpha,\phi,\omega)$ into Eq. (33) and using the same change of variable as before gives $G = \frac{4\pi}{cos\alpha_1}$. The normalized cross spectral density can be given as:

$$F_2(\alpha,\phi,\omega) = exp\left[\left(i\frac{\omega d}{c}\right)cos\alpha_1 cos\phi_1\right]$$

(45)

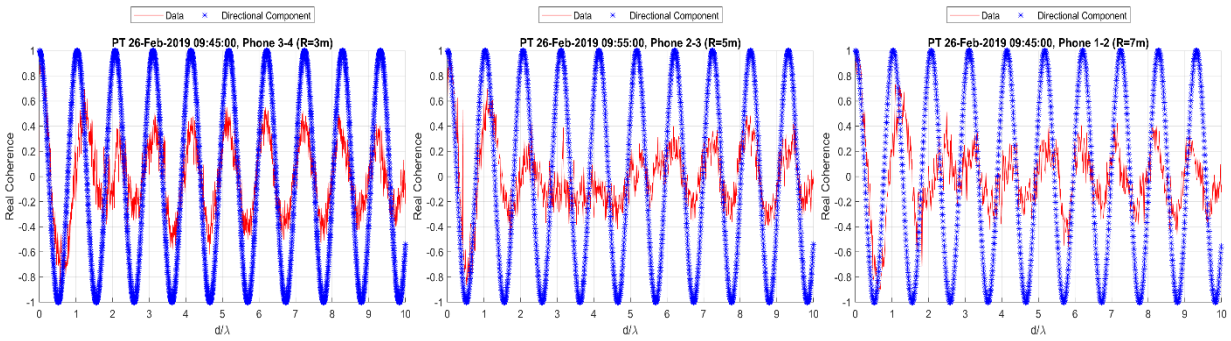

Figure 27: Comparison of the coherence functions from the directional component F_2 and the experimental data at 09:45 PT with $\alpha_1 = 0$ and $\phi_1 = 15$.

Figure 27 shows the coherence function for the directional component with $\phi_1 = 15$ that appears to match the data quite well for almost all of the zero crossings except for the first one and the last few. The coherence function is also at unity for the peaks, which exceeds the amplitude of the coherence function from the data. It is hypothesized that the 15° is attributed to the azimuth and not the elevation, as 15° in elevation for a receiver near the sea bottom would imply that the source is at a great distance away. As such, a convex combination of the two fields is needed to produce the overall noise field:

$$F(\alpha, \phi, \omega) = \sigma F_1(\alpha, \omega) + (1 - \sigma) F_2(\alpha, \phi, \omega)$$

(46)

where $0 \leq \sigma \leq 1$ is the weighting factor for the convex combination of the two fields, and $F_1(\alpha, \omega)$ is the azimuthally independent field that was defined in Eq. (38). By substituting Eq. (46) into Eq. (35) and setting $\gamma = \frac{\pi}{2}$, the cross spectral density is given by:

$$\rho\left(d, \omega; \frac{\pi}{2}\right) = \frac{\sigma}{2 sin\beta} \int_{-\beta}^{\beta} J_0 \left[\left(\frac{\omega d}{c}\right) cos\alpha\right] cos\alpha \, d\alpha + (1 - \sigma) exp\left[\left(i \frac{\omega d}{c}\right) cos\alpha_1 cos\phi_1\right]$$

(47)

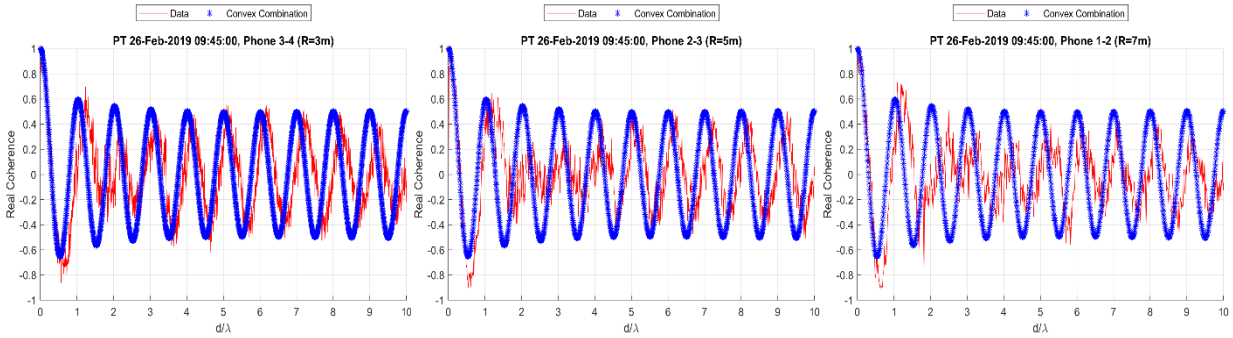

Figure 28: Comparison of the coherence functions from the combined noise field and the experimental data at 09:45 PT with $\sigma = 0.5$, $\alpha_1 = 0$ and $\phi_1 = 0$.

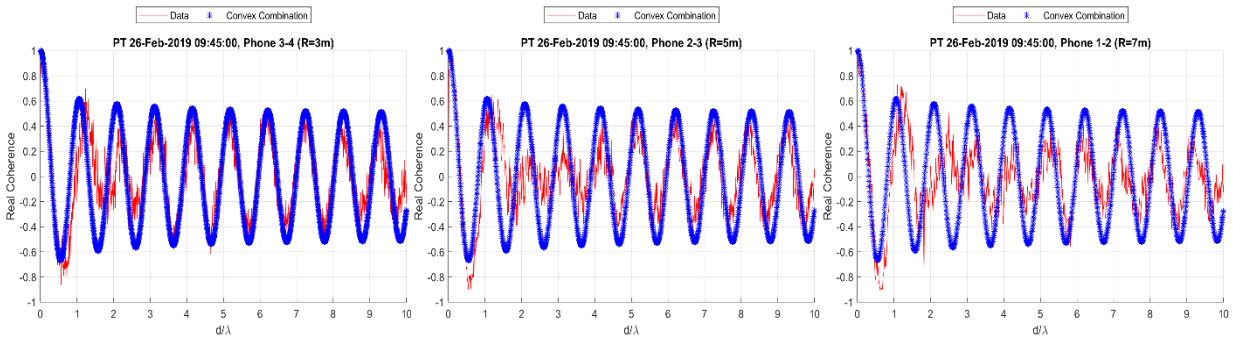

Figure 29: Comparison of the coherence functions from the combined noise field and the experimental data at 09:45 PT with $\sigma = 0.5$, $\alpha_1 = 0$ and $\phi_1 = 15$.

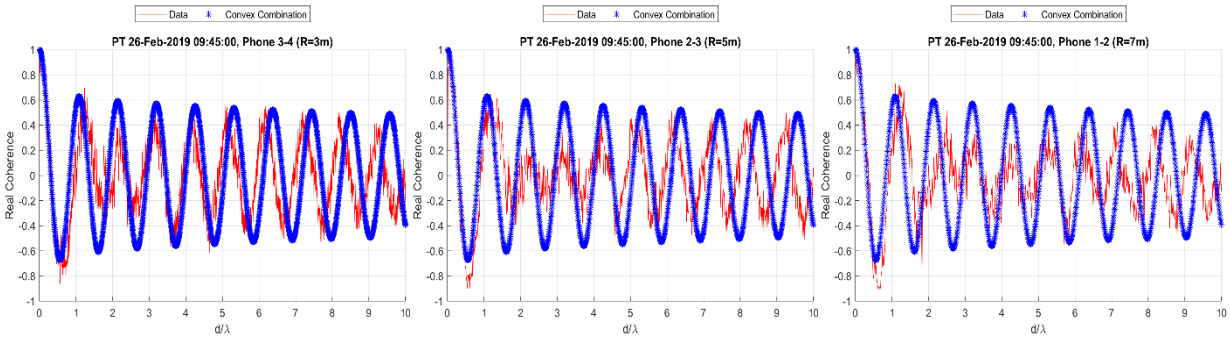

Figure 30: Comparison of the coherence functions from the combined noise field and the experimental data at 09:45 PT with $\sigma = 0.5$, $\alpha_1 = 0$ and $\phi_1 = 20$.

Figure 28, Figure 29 and Figure 30 show the coherence functions computed with by Eq. (47) for varying values of ϕ_1 while assuming that there is no elevation with $\alpha_1 = 0$ and that both noise field components are equally weighted. $\phi_1 = 0$ would imply that the directional component is propagating in a direction that is parallel to the line joining the hydrophones. It can be observed that the best fit is obtained with $\phi_1 = 15$, with the second and third zero crossings occurring at lower frequencies compared to same zeros in the data but otherwise matching the experimental data very well. It can be concluded that the additional source of coherence is coming from a direction that is almost parallel to the hydrophone array in azimuth and with no elevation.

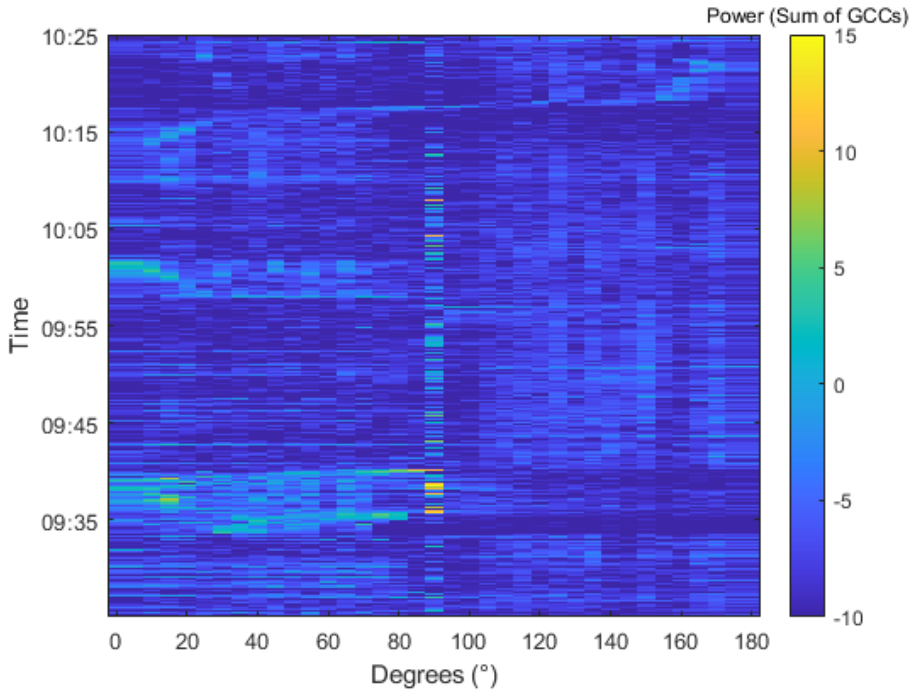

Figure 31: Plot of the Steered Response Power Phase Transform for the hydrophone data from the beginning of the experiment to the arrival of the helicopter.

To corroborate the existence of the additional source, the Steered Response Power Phase Transform (SRP-PHAT) [10] was used to compute the direction of arrival plot relative to the hydrophone array. For a given look direction, the SRP can be computed by applying the corresponding time shift to the generalized cross correlation (GCC) between all hydrophone pairs, and taking the Fourier transform to obtain the cross spectrum. To ensure that only the phase information is considered, the cross spectra for all hydrophone pairs are normalized by their magnitude. The resultant power for that specific look direction is obtained by summing the integral of all weighted cross spectra over all frequencies. This method was used in place of conventional beamforming as the wide hydrophone spacings would result in spatial aliasing when computing for the power at higher frequencies. Figure 31 shows the SRP-PHAT plot where 0° is pointing south towards the first hydrophone and 180° is pointing north towards the last hydrophone. There

are two periods of significant interference, where the first one occurred slightly after 9:35 am and the second one occurred after 9:55 am, both of which alters the coherence function plots significantly during those periods. The helicopter is also observable as it approached the first hydrophone from the south at 10:15 am, and a clear track could be seen as it reached the closest point of approach and head north. There was no noticeable source in the SRP-PHAT plot that was consistently present at $\phi_1 = 15$.

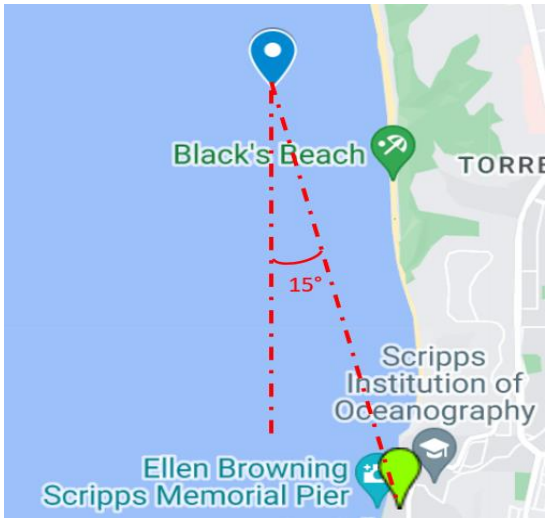

Figure 32: Map view obtained from Google Maps, with the blue pin indicating the position of the array and the green pin is located at a relative bearing of 165° from north at a distance of 3.6 km.

Figure 33: Photo taken of the SPROUL, a Scripps Research Vessel which was in the vicinity on that day. The La Jolla coastline can be seen in the background, and it might have been moving during the experiment.

According to the trial logs, there were only two vessels nearby. The first is the support boat which has powered down shortly after deploying the hydrophones. The second is the SPROUL, which is a Scripps research vessel shown in Figure 33. By drawing a line that is 15° from the south, the westward direction would lead further into the ocean, while the eastward direction would mark a location near the Ellen Browning Scripps Memorial Pier at a distance of 3.6 km as shown in Figure 32. This implies that the pier is a plausible source of interference as it has active water pumps that feed seawater to the Birch Aquarium and nearby facilities. even though it was not picked up by the SRP-PHAT plot

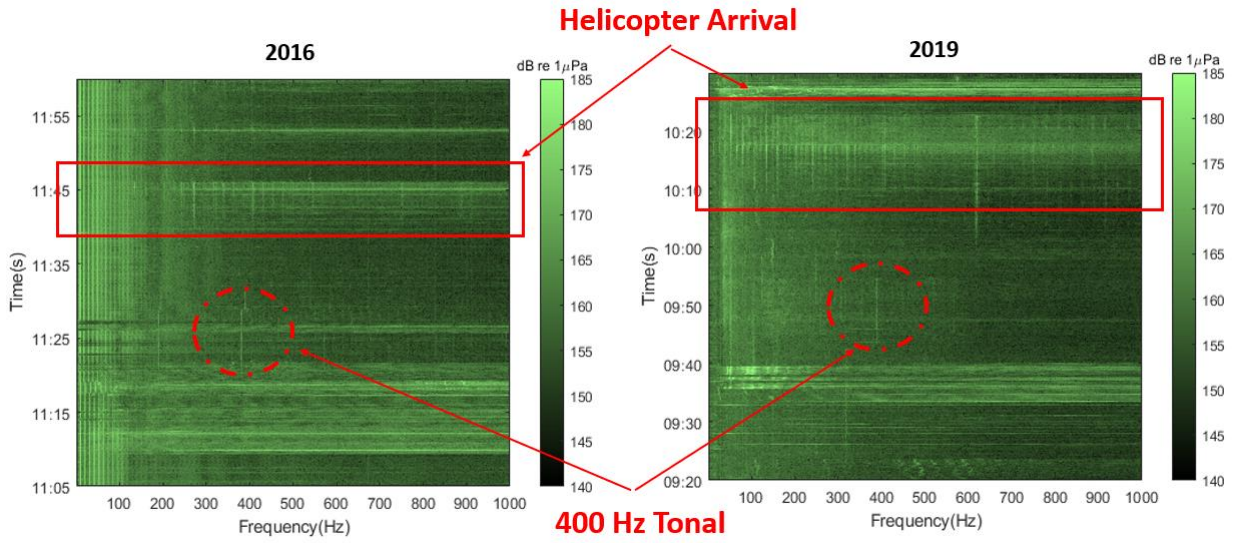

Figure 34: Spectrum plots for both the 2016 and 2019 experiment. There is a 400 Hz tonal lasting for approximately 15 minutes that is visible in both experiments.

The SPROUL might have also been positioned along the 15° line during the experiment. Further inspection with the spectrum plots shown in Figure 34 indicates that there are no visible frequency features that persist throughout both data sets. While there appears to be a 400 Hz tonal line that is visible in both experiments for roughly 15 minutes, it is not sufficient to explain the ambient noise coherence plots. Given the available information, the identity of the source at 15° remains inconclusive.

CHAPTER 4

Conclusion

This thesis report is a continuation of the investigation of the horizontal coherence function between two underwater sensors in the presence of an airborne source and is primarily based on the data collected during the 2019 experiment. The 2019 experiment was conducted with a hydrophone array with four hydrophones with a length of 15 m. The derived expression for the coherence function between two horizontally aligned sensors in Eq. (22) was a clear match for all six pairs of hydrophones when the helicopter was positioned to generate a dominant head wave that could be captured by the array, and the expression did not match well when the helicopter was not within the appropriate range window. The range window is defined by the critical angle on the sediment and the height of the helicopter, where a source that is far away would generate head waves that would have attenuated by the time it reaches the array, and a source that is too near would produce a head wave that is not detected by the array. The simulation performed with SCOOTER shows a mis-match with the experimental data when the source was only 10 m away, but otherwise agreed with the data when the source was further away and it validated the derived expression for all of the hydrophone pairs.

The least mean squares method was proposed as an alternative to extracting the zero crossings when it comes to deriving the sound speed. The least mean squares exploited the entire shape of the coherence curve and not just the zero crossing locations, and it provided better sediment sound speed estimates especially when plotted against normalized frequency.

Aside from measuring the coherence curves from the helicopter noise data, this thesis also investigated the coherence function for the ambient noise at the experiment site. The coherence

curves computed from the ambient noise data was compared with theoretical curves from various ocean noise models. For hydrophone spacings that are less than half the depth of the array, the isotropic noise model is a close fit in terms of the zero crossings despite the lower amplitude of the coherence function at higher frequencies. An alternative model that consisted of a convex combination of noise fields proved to be the best fit, where the first noise field is represented by ambient noise being restricted a sector within the critical angle and the second contribution came from a wave that is propagating in a direction that is at 15° from the south. By drawing a line from the hydrophone array, it is concluded that the second contribution might come from the active water pumps at the Ellen Browning Memorial Scripps Pier.

In summary, the thesis was successful in establishing the validity of the coherence function of the head wave for a separation of up to 15 m. The least squares fitting was also proposed as a better method for estimating the sediment sound speed, and the ambient noise for the experiment site was shown to be characterized by a convex combination of an azimuthally uniform noise field and a directional component.

REFERENCES

[1] R. J. Urick, "Noise signature of an aircraft in level flight over a hydrophone in the sea," *The Journal of the Acoustical Society of America,* vol. 52, no. 3B, pp. 993-999, 1972.

[2] H. Medwin, R. Helbig and J. Hagy, "Spectral characteristics of sound transmission through the Rough Sea Surface," *The Journal of the Acoustical Society of America,* vol. 54, no. 1, pp. 99-109, 1973.

[3] M. J. Buckingham and E. M. Giddens, "Theory of sound propagation from a moving source in a three-layer Pekeris waveguide," *The Journal of the Acoustical Society of America,* vol. 120, no. 4, pp. 1825-1841, 2006.

[4] M. J. Buckingham, E. M. Giddens, F. Simonet and T. R. Hahn, "Sound from a Light Aircraft for Underwater Acoustics Applications," *Proceedings of ICONS 2002. International Conference on Sonar – Sensors and Systems,* 2002.

[5] D. A. Bevans and M. J. Buckingham, "Estimating the sound speed of a shallow-water marine sediment from the head wave excited by a low-flying helicopter," *Journal of the Acoustical Society of America,* vol. 142, no. 4, pp. 2273-2287, 2017.

[6] M. B. Porter, "The KRAKEN normal mode program," *Report No. NRL/MR/5120-92-6920 Naval Research Laboratory, Washington, DC,* 1991.

[7] B. F. Cron and C. H. Sherman, "Spatial-Correlation Functions for Various Noise Models," *Journal of the Acoustical Society of America,* vol. 34, no. 11, 1962.

[8] H. Schmidt and F. B. Jensen, "A full wave solution for propagation in multilayered viscoelastic media with application to Gaussian beam reflection at fluid–solid interfaces," *The Journal of the Acoustical Society of America,* vol. 77, no. 813, 1985.

[9] H. Cox, "Spatial correlation in arbitrary noise fields with application to ambient sea noise," *Journal of the Acoustical Society of Americ,* vol. 54, no. 1289, 1973.

[10] J. H. DiBiase, "A High Accuracy, Low-Latency Technique for Talker Localization in Reverberant Environments using Microphone Arrays," *Brown University (Ph.D.),* 2000.